J. Fluid Mech. (2005), *vol.* 531, *pp.* 85–111.
doi:10.1017/S0022112005003800 Printed in the United Kingdom

Mode interaction and the bypass route to transition

By TAMER A. ZAKI AND PAUL A. DURBIN
Mechanical Engineering, Stanford University, Stanford, CA 94305-3030, USA

(Received 6 August 2003 and in revised form 13 December 2004)

The manner by which external vortical disturbances penetrate the laminar boundary layer and induce transition is explored. Linear theory suggests that the well-known Klebanoff mode precursor to transition can be understood as a superposition of Squire continuous modes. Shear sheltering influences the ability of free-stream disturbances to generate a packet of Squire modes. A *coupling coefficient* between continuous spectrum Orr–Sommerfeld and Squire modes is used to characterize the interaction. Full numerical simulations with prescribed modes at the inlet substantiate this approach. With two weakly coupled modes at the inlet, the boundary layer is little perturbed; with two strongly coupled modes, Klebanoff modes are produced; with one strongly coupled and one weakly coupled high-frequency mode, the complete transition process is simulated.

1. Introduction

The process by which free-stream vortical disturbances induce transition to turbulence in an underlying boundary layer, without the intervention of viscous Tollmien–Schlichting instability waves, is called bypass transition. A good deal of information about bypass transition is available from experiments and computer simulations (Westin *et al.* 1994; Jacobs & Durbin 2000). Transition is preceded by the formation of velocity perturbations that are very long in the streamwise direction. They can be regarded as forward and backward jets in the perturbation field. These are probably what originally were called 'breathing modes' (Klebanoff 1971), and what Kendall (1991) named 'Klebanoff modes'. They are not modes, in the sense of being eigenfunctions of a response equation. They have been explained as displacements of mean momentum. Their long streamwise extent can be understood by rapid distortion theory: this theory shows that disturbances with small streamwise wavenumber k_x are subjected to prolonged growth by lift-up of momentum, without producing a restoring pressure (Phillips 1969).

However, the process by which disturbances enter the boundary layer, prior to their amplification by lift-up, has been a matter of uncertainty and speculation. One proposal is that disturbances enter in the highly non-parallel leading-edge region. Because the boundary layer is quite stable in that region, a process of vortex stretching around the leading edge has been included in this idea (Goldstein & Wundrow 1998). But, computer simulations reproduce bypass transition without mediation by a leading edge.

1.1. *Local receptivity*

It is suggested in Jacobs & Durbin (2000) that external disturbances penetrate the boundary layer locally, rather than entering at the leading edge. Inviscid theory does

not allow such penetration: convected free-stream disturbances are sheltered by the shear (Hunt & Durbin 1999). However, viscous theory shows that low Reynolds number, low frequency, or sufficiently oblique free-stream disturbances can penetrate the boundary layer. This behaviour is described by the continuous spectrum of the Orr–Sommerfeld equation (Grosch & Salwen 1978; Gustavsson 1979).

The role of the continuous eigenfunctions is only uncovered by examining mode shapes. Continuous Orr–Sommerfeld and Squire eigenfunctions are oscillatory in the free stream. Inside the boundary layer their amplitude decays toward the wall. The rate of fall off with distance from the top of the boundary layer depends on the particular mode. Each mode has a particular depth to which it penetrates the boundary layer. The extent of penetration is locally limited by the shear. The concept of shear sheltering (Hunt & Durbin 1999) provides an understanding of this aspect of mode shapes, and of the ability of free-stream disturbances to locally penetrate the boundary layer.

The present idea of local interaction is consistent with an observation made by Leib, Wundrow & Goldstein (1999). In that paper, disturbances inside the boundary layer were described by the boundary-region equations. The boundary-region equations are elliptic in the cross-flow plane. Conditions at the outer edge of the boundary layer locally induce a disturbance in the shear layer.

1.2. *Penetration depth and the coupling coefficient*

Jacobs & Durbin (1998) define a 'penetration depth', d, modelled on the solution for a piecewise linear shear layer. The solution in that case is an Airy function, which oscillates periodically in the free stream and decays exponentially in the shear layer, similar in form to the eigensolutions for the Blasius profile. Computed shapes were characterized by the penetration depth, and the formula $d \propto (\omega R)^{-0.133}$ provided an approximate fit to the computed shapes. This formula is suggestive of the Reynolds number and frequency dependence.

However, Jacobs & Durbin (1998) measured penetration depth rather subjectively. They also restricted attention to a single wall-normal wavenumber, k_y. Further mode calculations show that larger k_y disturbances oscillate deeper into the boundary layer and the simplistic idea of penetration requires revision.

In this paper, we propose a more suitable characterization. Three-dimensional continuous Orr–Sommerfeld modes force Squire's equation resonantly (Hultgren & Gustavsson 1981). The forcing can be characterized by a coupling coefficient, which is defined as the inner product of an adjoint Squire eigenfunction with the forcing term. This can be thought of as a measure of the propensity for continuous-spectrum Orr–Sommerfeld eigenfunctions to generate breathing modes. Countering this is the viscous decay. Thus, our coupling coefficient Θ is normalized by the modal decay rate. Larger values of Θ define penetrating modes, in the present broadened sense. Smaller values are non-penetrating.

The coupling coefficient is based on local boundary layer scales. It is interesting to contrast the penetration characteristics of free-stream disturbances at different downstream locations. Close to the leading edge, the boundary layer thickness is small, all non-dimensional frequencies are low, and hence all modes are penetrating. Farther downstream, based on the local boundary layer scaling, some modes become high frequency and hence are sheltered by the shear. This is consistent with the local interactions suggested in the numerical studies of Leib *et al.* (1999) and Jacobs & Durbin (2000).

Although the coupling coefficient represents penetration depth, it addresses other aspects of the interaction too. The extent of penetration enters because the velocity gradient appears in the integral that defines Θ. The coupling coefficient also recognizes that Squire modes are only forced by oblique Tollmien–Schlichting waves. Two-dimensional waves penetrate, but their coupling coefficient vanishes. Disturbances with large k_y enter the boundary layer, but they are strongly damped by viscous decay, so have a small coupling coefficient.

The use of a single, resonant, Squire mode to define the interaction is somewhat misleading. A single Orr–Sommerfeld wave forces all Squire modes, for the following reason. Continuous-spectrum Squire eigenfunctions are oscillatory in the free stream. Because they are the vertical component of vorticity, η, which is produced when an Orr–Sommerfeld mode distorts the mean vorticity, a single mode cannot be produced by Orr–Sommerfeld forcing: there is no source for the oscillatory free-stream vorticity. This physical observation is illustrated by the initial value problem $\eta = 0$ at $t = 0$; its solution shows that all Squire modes are generated, and in the free stream they sum to zero (see the Appendix and Schmid & Henningson 2001). This response is a superposition of modes, not a single resonant mode.

At high forcing frequency, Squire modes are non-penetrating, and their perturbation vanishes inside the boundary layer; for low-frequency forcing, Squire modes do not vanish within the boundary layer. This is due to the variation of shear sheltering with k_y. Breathing modes, then, should be considered to be the incomplete cancellation that occurs within the boundary layer. Penetrating resonant Squire modes may well be the origin of transition; however, it is the incomplete cancellation of a packet of Squire modes that causes the breathing modes to emerge.

Klebanoff modes are a prerequisite of bypass transition as observed experimentally (Kendall 1991) and in numerical simulations (Jacobs & Durbin 2000). Their growth has been extensively addressed in the literature – indeed, some of the analysis goes back to the 1960s and 1970s (Phillips 1969). Recognizing that breathing, or Klebanoff, modes are not eigensolutions, and can be regarded as a superposition, shifts our focus from them to a study of more fundamental Orr–Sommerfeld and Squire mode interactions.

1.3. *Mode interaction and bypass transition*

The present study of mode interactions provides a framework for addressing the bypass problem in a manner similar to that of orderly transition. The proposed relation between the continuous spectrum and bypass transition suggests an analogy to the relation between Tollmien–Schlichting waves and orderly transition. In the latter context, nonlinearity and interactions between eigenmodes have been studied extensively – see the review by Kleiser & Zang (1991). These studies have elucidated many aspects of orderly transition. That motivates us to initiate similar studies of the nonlinear development of continuous modes. The picture is less clear than for orderly transition, but the analogy does seem fruitful. The present paper describes computer simulations of the nonlinear mode development.

Our direct numerical simulations (DNS) are of pairwise mode interaction. The evidence presented herein supports the idea that penetration and nonlinear interaction are key elements of the transition process. In the simulations, two Orr–Sommerfeld modes are prescribed at the inlet. The inflow plane is chosen far enough upstream to contain the interaction. It is upstream of the zone of the boundary region equations denoted III in Leib *et al.* (1999, figure 1). Hence, the region to which those authors attributed great significance is contained within our domain. However, the evolution of

modes is here computed by DNS, so nonlinear interaction and non-parallel effects are included fully. Our domain extends beyond the boundary region zone, into transition.

If both modes specified at the inlet are penetrating, perturbation jets appear, but do not transition within the computational domain. If neither is penetrating, they simply decay. Only the case of one penetrating and one non-penetrating leads to transition in our computer experiments. This is consistent with the theory of Jacobs & Durbin (2000): backward perturbation jets are generated by penetrating modes and correspond to Klebanoff or 'breathing' modes. They are associated with upward displacement of fluid elements. When the jets approach the top of the boundary layer, they are subject to inflection point instability, triggered by higher frequency non-penetrating disturbances. The instability of these elevated shear regions results in the inception of turbulent spots. An analogy can be drawn with natural transition where the high-frequency oscillations commence in shear regions located at $y/\delta^* \approx 0.6$ (Kleiser & Zang 1991, figures 4 and 5). Hence, both high- and low-frequency disturbances are needed. We find herein that an inlet with *just two* modes, of this ilk, suffices to produce bypass transition.

2. The Orr–Sommerfeld/Squire eigenvalue problem

The equations governing small disturbances about a parallel viscous mean flow $U(y)$ can be reduced into the following pair, for the normal velocity v and vorticity η (Drazin & Reid 1995):

$$\partial_t \begin{bmatrix} v \\ \eta \end{bmatrix} = \begin{bmatrix} \Delta^{-1}\left\{d_y^2 U \partial_x + (R^{-1}\Delta - U\partial_x)\Delta\right\} & 0 \\ -d_y U \partial_z & R^{-1}\Delta - U\partial_x \end{bmatrix} \begin{bmatrix} v \\ \eta \end{bmatrix} \tag{2.1}$$

where Δ is the Laplacian operator, and Δ^{-1} is the formal inverse. Lengths are non-dimensionalized by the boundary layer 99% thickness, δ, and velocities by the free-stream speed, U_∞, so that $R = U_\infty \delta/\nu$. (We will subsequently include U_∞ in equations, for clarity, although it is unity.)

To solve the system (2.1), Fourier representations can be invoked in the homogeneous streamwise and spanwise directions, as well as in time:

$$\begin{bmatrix} v(\boldsymbol{x}, t) \\ \eta(\boldsymbol{x}, t) \end{bmatrix} = \begin{bmatrix} \phi(y) \\ \chi(y) \end{bmatrix} \mathrm{e}^{\mathrm{i}(k_x x + k_z z - \omega t)}.$$

The governing equations are then reduced to the Orr–Sommerfeld/Squire eigenvalue problem

$$-\mathrm{i}\omega \begin{bmatrix} \phi(y) \\ \chi(y) \end{bmatrix} = \begin{bmatrix} \mathscr{L} & 0 \\ -\mathscr{C} & \mathscr{S} \end{bmatrix} \begin{bmatrix} \phi(y) \\ \chi(y) \end{bmatrix} \tag{2.2}$$

where

$$\begin{aligned} \mathscr{L} &= \Delta^{-1}\left\{\mathrm{i}k_x U'' + [\Delta(\Delta)/R] - \mathrm{i}k_x U \Delta\right\}, \\ \mathscr{S} &= [(\Delta/R) - \mathrm{i}k_x U], \\ \mathscr{C} &= \mathrm{i}k_z U'. \end{aligned}$$

The solution to the Orr–Sommerfeld equation when y ranges from 0 to ∞ consists of a discrete spectrum, with eigenvalues ω_n, $n = 1, 2, 3 \ldots N$, and a continuous spectrum ω_{k_y}. The eigenfunctions satisfy $\lim_{y\to\infty} \phi_n$, $\chi_n(y) = 0$, $\lim_{y\to\infty} \phi_{k_y}$, $\chi_{k_y}(y)$ bounded. The latter are oscillatory in the free stream and provide a Fourier basis for disturbances (Grosch & Salwen 1978).

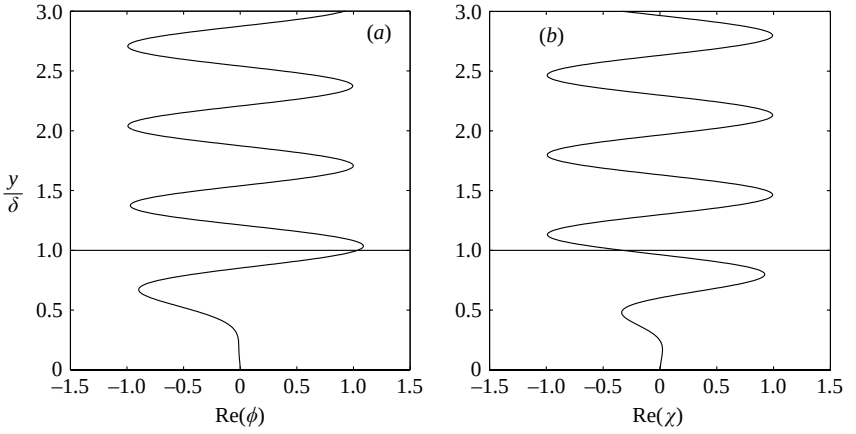

FIGURE 1. Example of continuous (*a*) Orr–Sommerfeld and (*b*) Squire modes. $R = 100$, $\omega = \pi$, $k_y = 3\pi$, $k_z = \pi$.

In optimal growth analysis (Schmid & Henningson 2001), the pair of equations (2.2) is regarded as a coupled eigensystem, with non-normal eigenfunctions – due primarily to the coupling term $\mathscr{C}$. We adopt the alternative view that

$$-\begin{bmatrix} \mathrm{i}\omega_{os}\phi \\ \mathrm{i}\omega_{sq}\chi \end{bmatrix} = \begin{bmatrix} \mathscr{L} & 0 \\ 0 & \mathscr{S} \end{bmatrix} \begin{bmatrix} \phi \\ \chi \end{bmatrix}. \tag{2.3}$$

In this formulation, the relevant eigenvalue problems are the Orr–Sommerfeld and homogeneous Squire's – which are decoupled, and both eigenfunctions can be independently normalized. Shape characteristics of the continuous spectra explain the local interaction of free-stream disturbances with the boundary layer (figure 1).

Also, the coupling term, $\mathscr{C}$, is not a non-normal contribution in the eigenvalue problem (2.3). Instead, it is included as a forcing term in the normal vorticity equation

$$\left(\frac{\Delta}{R} - U\partial_x\right)\eta - \partial_t\eta = \mathscr{C}\phi \mathrm{e}^{\mathrm{i}(k_x x + k_z z - \omega_{os} t)}. \tag{2.4}$$

The solution to the initial value problem $\eta = 0$ at $t = 0$ is given in the Appendix (see also Hultgren & Gustavsson 1981). The vertical vorticity equation (2.4) is solved as a forced response problem, with the vertical velocity being a known forcing function. If the forcing is not orthogonal to the homogeneous Squire eigenfunctions, it will generate secular growth; that is the analogue to non-normality.

3. Resonance in the eigenvalue problem

Consider the Orr–Sommerfeld operator

$$\left[\left(\frac{\mathrm{d}^2}{\mathrm{d}y^2} - k_x^2 - k_z^2\right)^2 - \mathrm{i}k_x R\left\{(U-c)\left(\frac{\mathrm{d}^2}{\mathrm{d}y^2} - k_x^2 - k_z^2\right) - \frac{\mathrm{d}^2 U}{\mathrm{d}y^2}\right\}\right]\phi = 0. \tag{3.1}$$

The continuous spectrum was obtained in Grosch & Salwen (1978). In the free stream, $U(y) = U_\infty$, and $\mathrm{d}^2U/\mathrm{d}y^2 = 0$. Therefore, the eigenvalue problem reduces to

$$\left[\left(\frac{\mathrm{d}^2}{\mathrm{d}y^2} - k_x^2 - k_z^2\right)^2 - \mathrm{i}k_x R\left\{(U_\infty - c)\left(\frac{\mathrm{d}^2}{\mathrm{d}y^2} - k_x^2 - k_z^2\right)\right\}\right]\phi = 0 \tag{3.2}$$

which admits solutions of the form $\phi \sim \mathrm{e}^{\lambda y}$. Substituting and solving for λ yields four roots:

$$\lambda_{1,2}^2 = k_x^2 + k_z^2 + \mathrm{i}k_x R(U_\infty - c),$$
$$\lambda_{3,4}^2 = k_x^2 + k_z^2.$$

The last two roots are a decaying and a growing exponential. The latter is rejected as non-physical. The first two roots are oscillatory modes in the free stream $\phi \sim \mathrm{e}^{\pm \mathrm{i}k_y y}$, upon setting $\lambda_{1,2}^2 = -k_y^2$. This gives the dispersion relation for the Orr–Sommerfeld continuous spectrum:

$$k_x^2 + k_y^2 + k_z^2 + \mathrm{i}k_x R(U_\infty - c) = 0. \tag{3.3}$$

Equation (3.3) can be solved for the temporal

$$\omega = k_x U_\infty - \frac{\mathrm{i}}{R}\left(k_x^2 + k_z^2 + k_y^2\right) \tag{3.4}$$

or spatial

$$k_x^r = \omega\left[\sqrt{M^2 + \frac{4\omega^2}{R^2}} + M\right]^{-1/2}, \qquad k_x^i = \frac{R}{2}\left[\frac{\omega}{k_x^r} - 1\right] \tag{3.5}$$

eigenvalues. Here

$$M = \frac{1}{2} + \frac{2\left(k_y^2 + k_z^2\right)}{R^2}.$$

It is easy to see that the dispersion relation for the homogeneous Squire operator is identical to the dispersion relation of the Orr–Sommerfeld equation. Substituting $U(y) = U_\infty$ in the free stream, and $\chi \sim \mathrm{e}^{\pm \mathrm{i}k_y y}$, into the second of (2.3) gives the dispersion relation

$$k_x^2 + k_y^2 + k_z^2 + \mathrm{i}k_x R(U_\infty - c) = 0 \tag{3.6}$$

for the homogeneous Squire operator, as was the case in (3.3). Therefore, the temporal and spatial eigenvalues of the Squire operator are identical to their counterpart Orr–Sommerfeld operator and a possibility of resonant forcing exists. Such resonance gives rise to secular growth in the solution to the initial/boundary value problem. Hultgren & Gustavsson (1981) have previously commented on the role of direct resonance in the linear initial value problem; however, they were concerned with temporal growth, rather than with coupling to free-stream disturbances. Here we are concerned with coupling, and spatial growth is computed by full DNS.

4. Shear sheltering, mode shape, and penetration depth

In the limit of large Reynolds number, the phase velocity of the continuous modes equals the free-stream velocity. In the free stream, these disturbances are convected with the flow, and do not have an associated pressure disturbance. However, near the edge of the boundary layer, a pressure perturbation exists, and it provides a mechanism for the disturbance to penetrate the boundary layer. The penetration depth is determined by a balance between pressure gradient and the effect of shear. The latter inhibits the penetration of disturbances into the boundary layer – this phenomena is called *shear sheltering* (Hunt & Durbin 1999).

The physical mechanism of shear sheltering is important in understanding the local interaction of free-stream disturbances with the boundary layer. Only perturbations

not susceptible to the shear filtering effect can induce a response within the boundary layer. For example, contrast the Orr–Sommerfeld modes of figure 4. The highest frequency mode is expelled from the boundary layer by the shear, while the lowest frequency perturbation penetrates deep within the boundary layer. Only the latter Orr–Sommerfeld forcing can be the origin of breathing modes.

Shear sheltering also defines the shape of the boundary layer response to a penetrating perturbation. According to the solution of the initial value problem described in the Appendix, a single Orr–Sommerfeld wave forces a complete k_y spectrum of Squire modes, and in the free stream they sum to zero. A non-penetrating Orr–Sommerfeld forcing is not interesting because the corresponding Squire spectrum is also sheltered. For penetrating Orr–Sommerfeld forcing, the Squire wave packet still vanishes in the free stream, but not within the boundary layer. This is due to the variation of penetration depth with k_y. Some k_y components do not penetrate the shear, and hence only contribute to cancellation in the free stream. These components will not cancel the boundary layer disturbance. It is the incomplete cancellation of a packet of Squire modes that causes the breathing modes to emerge. One might cite an analogy with the phase cancellation to which Butler & Farrell (1992) attribute some aspects of transient growth. In that case, initial conditions can be chosen such that disturbances amplify due to dispersive propagation. However, that phenomenology is very different from the present shear sheltering mechanism.

Hence, the role of shear sheltering is twofold: it 'selects' the penetrating Orr–Sommerfeld forcing, and defines the shape of the Squire response. An understanding of shear sheltering is therefore important when studying the local interaction of free-stream disturbances with the boundary layer. In the next subsection, the effect of shear on mode shape is studied using the model problem of a piecewise-linear velocity profile. The deductions of the simple model are then compared to numerical evaluation of the Orr–Sommerfeld and Squire eigenfunctions for a Blasius base flow.

4.1. *Solution for a linear velocity profile*

The continuous spectra of the Orr–Sommerfeld and homogeneous Squire eigenvalue problems exhibit similar penetration characteristics in the presence of shear. This resemblance is expected intuitively, since it originates in the velocity profile, and the uniform free-stream velocity. Analytically, a connection can be drawn by considering the Orr–Sommerfeld equation for a piecewise-linear base flow:

$$\left[\left(\frac{\mathrm{d}^2}{\mathrm{d}y^2}-\left(k_x^2+k_z^2\right)\right)^2-\mathrm{i}k_xR\left\{(U-c)\left(\frac{\mathrm{d}^2}{\mathrm{d}y^2}-\left(k_x^2+k_z^2\right)\right)\right\}\right]\phi=0. \tag{4.1}$$

A simple change of variables to $\psi=\Delta\phi=\phi''-(k_x^2+k_z^2)\phi$ transforms the three-dimensional fourth-order Orr–Sommerfeld equation to

$$\psi''-\left[\left(k_x^2+k_z^2\right)+\mathrm{i}k_xR(U(y)-c)\right]\psi=0 \tag{4.2}$$

which is identical to Squire's homogeneous problem.

Jacobs & Durbin (1998) solved the model problem of a two-dimensional Orr–Sommerfeld disturbance about a piecewise-linear velocity profile (figure 2)

$$\begin{aligned} U(y)&=U_\infty, && y>0,\\ U(y)&=U_\infty+\tau y, && y<0. \end{aligned}$$

They invoked the simplifying assumptions $k_x^i\approx 0$ and $c=\omega/k_x\approx U_\infty$. In this limit, and in the more general case of a three-dimensional disturbance, the solution to the

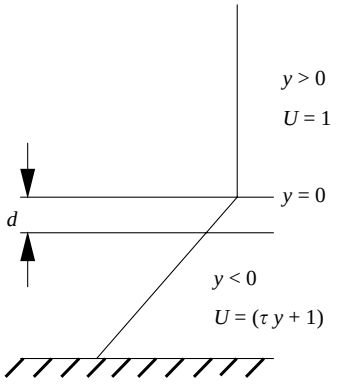

FIGURE 2. Model problem for shear sheltering.

governing equation (4.2) is

$$\psi(y) = A\mathrm{e}^{-Q^{1/2}y} + B\mathrm{e}^{+Q^{1/2}y}, \qquad y > 0,$$
$$\psi(y) = c_1 \mathrm{Ai}\left[(\mathrm{i}\omega R\tau)^{1/3}\left(y - \frac{\mathrm{i}(\omega^2 + k_z^2)}{R\omega\tau}\right)\right], \quad y < 0,$$

where $Q = -(k_x^2 + k_z^2) - \mathrm{i}k_x R(U_\infty - c)$. This solution resembles the continuous modes for the Blasius profile (figure 1). In the free stream, $y > 0$, the solution is oscillatory. Within the sheared region $y < 0$, the oscillations persist for $|y| \sim O((\omega^2 + k_z^2)/R\omega\tau)$. It is clear that stronger shear τ and higher Reynolds number both reduce the penetration of oscillatory solutions into the boundary layer. In the limit $|y| \gg (\omega^2 + k_z^2)/R\omega\tau$, the exponential decay is dominant,

$$\psi(y) \sim \frac{\exp\left((\mathrm{i} - 1)\frac{1}{3}\sqrt{2}\sqrt{\omega R\tau}\,|y|^{3/2}\right)}{|y|^{1/4}}. \tag{4.3}$$

The effect of k_y on penetration depth does not appear in the above solution due to the assumption $c \approx U_\infty$, which neglects the decay rate.

The dependence on k_y was not discussed by Jacobs & Durbin (1998). Increasing k_y results in an increase in the pressure gradient,

$$\frac{\mathrm{D}v}{\mathrm{D}t} = -\mathrm{i}k_y p$$

thus allowing the disturbance to penetrate further into the boundary layer. In order to include the effect of k_y on the penetration depth, the above analysis is repeated, accounting for the imaginary component of the phase speed c_i, which is responsible for decay. The solution inside the shear region can still be expressed in terms of the Airy function:

$$\psi(y) = c_1 \mathrm{Ai}\left[(\mathrm{i}\omega R\tau)^{1/3}\left(y + \frac{\mathrm{i}k_y^2}{R\omega\tau}\right)\right], \quad y < 0. \tag{4.4}$$

When $|y| < k_y^2/R\omega\tau$, the argument of the Airy function has negative real part, and the solution is oscillatory. However, as $|y|$ becomes larger ($|y| > k_y^2/R\omega\tau$), a decaying solution is obtained. Therefore, including the decay rate (the complex part of the phase speed) illustrates how the larger k_y modes remain oscillatory well into the shear

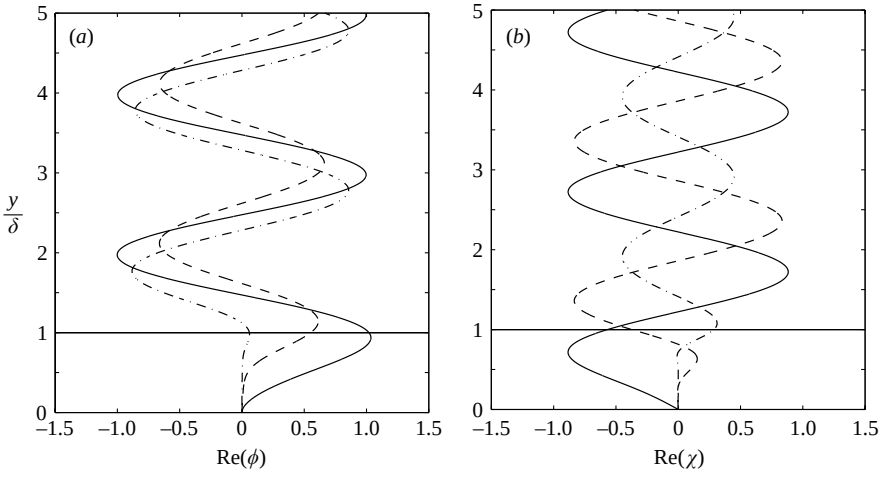

FIGURE 3. Effect of R on penetration depth ($\omega = \pi, k_z = \pi, k_y = \pi$): ——, $R = 10$; - - -, $R = 100$; — · —, $R = 1000$. (*a*) Orr–Sommerfeld modes and (*b*) Squire modes.

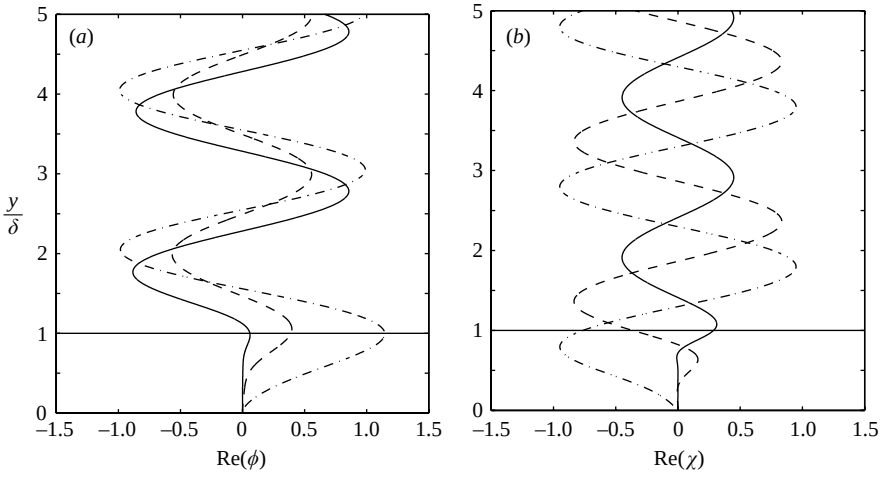

FIGURE 4. Effect of ω on penetration depth ($R = 1000, k_z = \pi, k_y = \pi$): ——, $\omega = \pi$; - - -, $\omega = \pi/10$; — · —, $\omega = \pi/100$.

region. The solution also captures the effect of ω, τ, and R on penetration depth. All three parameters are inversely proportional to penetration according to (4.4).

4.2. *Numerical solution*

The above deductions based on a piecewise-linear profile are here verified by comparison to the numerical solutions of the Orr–Sommerfeld and Squire eigenvalue problems for a Blasius profile. The numerical results show dependence of shear sheltering on Reynolds number R, frequency ω, and wall-normal wavenumber k_y. Consider the continuous modes shown in figures 3 and 4. The effect of increasing R, and therefore the shear, is clearly to reduce the penetration of disturbances into the boundary layer. Similarly, modes with higher frequency, ω, experience enhanced shear filtering. These results are consistent with the analytical predictions from equation (4.4). While the low-R eigenfunctions in figure 3 at first might seem uninteresting,

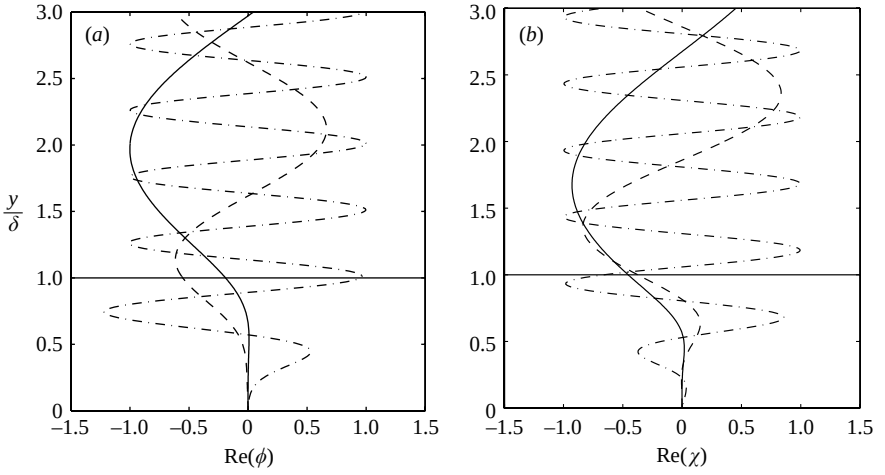

FIGURE 5. Effect of k_y on penetration depth ($R = 100, \omega = \pi, k_z = \pi$): ——, $k_y = \pi/2$; - - -, $k_y = \pi$; — · —, $k_y = 4\pi$.

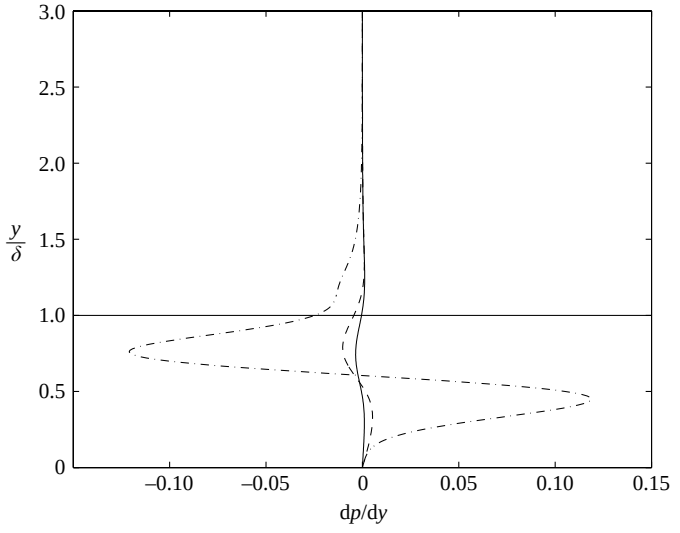

FIGURE 6. Effect of k_y on wall-normal pressure gradient.

Squire's transformation makes them relevant to oblique modes at higher Reynolds number.

Also notable is the similarity of the penetration characteristics of the Tollmien–Schlichting modes to the corresponding Squire eigenfunctions. A Squire spectrum, forced by a non-penetrating Orr–Sommerfeld perturbation, is also non-penetrating. These results suggest that low-frequency Orr–Sommerfeld modes are more effective at perturbing the boundary layer, and generating normal vorticity.

The dependence on k_y is curious. Consider the results of figures 5 and 6. The disturbance pressure gradient is enhanced for larger k_y. As a result, the perturbation penetrates deeper into the boundary layer, consistent with the theoretical prediction for a piecewise-linear profile. Hence, short-wavelength disturbances remain oscillatory well into the boundary layer as shown in figure 5. However, the improvement of

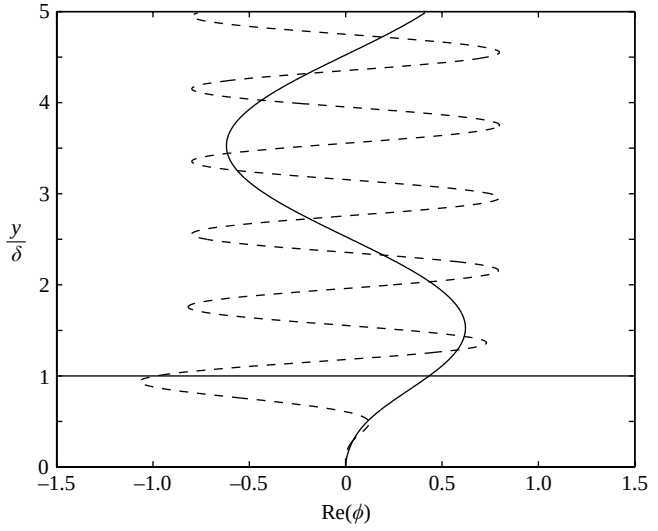

FIGURE 7. Penetration depth alone is not a sufficient measure of disturbance effectiveness, shown by two modes at ($R = 1000, k_z = \pi$): mode 1 (——, $\omega = \pi/50, k_y = \pi/2$) has much lower decay rate than mode 2 (- - -, $\omega = \pi/10, k_y = 5\pi/2$).

penetration depth is at the expense of an increased decay rate; see equations (3.4), (3.5). As a result, one expects the existence of an optimal k_y for which the Orr–Sommerfeld forcing penetrates deep into the boundary layer, while maintaining a reasonable decay rate. Forcing at lower wall-normal wavenumber would be filtered by the shear, and modes with higher k_y would decay quickly and not persist far downstream of the leading edge.

The dependence of shear sheltering on k_y is more interesting when discussing the response to a penetrating Orr–Sommerfeld forcing. The solution to the initial value problem $\eta = 0$ at $t = 0$ requires that the generated Squire spectrum sums to zero in the free stream. However, the dependence of shear sheltering on k_y results in a finite disturbance inside the boundary layer – the breathing modes.

4.3. *Penetration depth*

Shear sheltering is a physical mechanism, perhaps the only one capable of explaining the variation of mode shape inside the boundary layer. It is therefore important in understanding the local interaction of free-stream disturbances with the boundary layer. The filtering effect of shear also explains the different behaviours of the solution to the initial value problem in the shear layer and the free stream. A superposition of eigenfunctions that cancels in the free stream can have a large amplitude in the shear region because different modes have different penetration characteristics, depending on the wavenumber and frequency. In that sense, the physical mechanism of shear sheltering defines the shape of Klebanoff or 'breathing' modes.

In order to quantify the sheltering effect of shear, or the effectiveness of disturbances in penetrating the boundary layer, a concept of *penetration depth* was proposed in Jacobs & Durbin (1998). For example, one might measure the distance into the boundary layer where the disturbance has decayed to a specified level. Evaluating penetration depth in this way is subjective, especially for modes which continue to oscillate inside the boundary layer while also decaying.

Another limitation is the failure to characterize the persistence of modes. For instance, consider the two modes of figure 7: both penetrate to a comparable depth

into the boundary layer. But the mode with larger k_y has a much larger viscous decay rate k_x^i. As a result, it is less effective at perturbing the boundary layer. This example demonstrates that penetration depth, *per se*, is not an ideal measure of the effectiveness of excitations at perturbing the boundary layer. For this purpose, the concept of a coupling coefficient is introduced in the next section. This coefficient will still include the idea of penetration, but it goes further in characterizing the degree of local interaction between free-stream disturbances and the boundary layer.

5. Coupling coefficient

If $\chi_{\omega_{sq}}$ solves the eigenvalue problem (2.3), then the forced equation

$$\left(\frac{\Delta}{R} - U\partial_x\right)\eta - \partial_t\eta = \mathscr{C}\phi e^{i(k_x x + k_z z - \omega_{os} t)} \tag{5.1}$$

has a secular solution because ω_{os} is also an eigenvalue to Squire's equation – unless a non-secularity condition is satisfied. The adjoint Squire operator is defined by (Schmid & Henningson 2001)

$$\langle \mathscr{S}^\dagger \chi^\dagger, \chi\rangle = \langle \chi^\dagger, \mathscr{S}\chi\rangle$$

where $\langle f, g\rangle \equiv \int_0^\infty f^* g\,\mathrm{d}y$ and the adjoint eigenfunction satisfies $\mathscr{S}^\dagger\chi^\dagger = i\omega_{sq}^*\chi^\dagger$. The non-secularity condition is

$$\langle \chi^\dagger, \mathscr{C}\phi\rangle = 0.$$

This can be seen by solving an initial value problem, as in the Appendix. In general, that inner product will not vanish; we use it to define the coupling coefficient.

The amplitude of the secular growth is determined by two competing factors. The forcing $\langle \chi_{k_y}^\dagger, \mathscr{C}\phi(y)\rangle$ favours growth: it represents the coupling between the Orr–Sommerfeld forcing and the Squire modes inside the boundary layer. The exponential factor $e^{\omega_{os}^i t}$ represents viscous decay. A combination of these can be used to quantify the effectiveness of Orr–Sommerfeld forcing in exciting Squire response. One possible combination, our proposed *coupling coefficient*, Θ, is

$$\Theta \equiv \left|\frac{-i\langle \hat{\chi}^\dagger, \mathscr{C}\hat{\phi}\rangle}{\omega_{os}^i}\right| = \left|k_z \frac{\langle \hat{\chi}^\dagger, U'\hat{\phi}\rangle}{\omega_{os}^i}\right|, \tag{5.2}$$

where $\hat{\phi}$ and $\hat{\chi}^\dagger$ are the Orr–Sommerfeld and adjoint Squire eigenfunctions, normalized to unit maximum amplitude in the free stream:

$$\max\ |\hat{\phi}(y)|_{y\to\infty} = \max\ |\hat{\chi}^\dagger(y)|_{y\to\infty} = 1.$$

This choice of normalization is motivated by the notion of 'coupling'. In order to compare the coupling of different modes, their free-stream amplitude must match.

Using the definition of Θ, compare the two modes of figure 7: both have comparable values of the inner product, $\langle \hat{\chi}^\dagger, U'\hat{\phi}\rangle \sim 0.02$, and penetration depth. However, the high-k_y mode has a lower coupling coefficient, $\Theta = 0.78$, versus 5.8 for the lower k_y, due to their different decay rates.

5.1. *Properties of the coupling coefficient, Θ*

The coupling coefficient was evaluated over a range of k_y and k_z, for $k_x = 0.32$. The contours in figure 8 show an optimal value at $k_y = 4.4$, $k_z = 5.1$. The optimum in wall-normal wavenumber occurs because k_y has the dual effect of increasing the inner product term, through enhanced penetration depth, and augmenting the decay rate

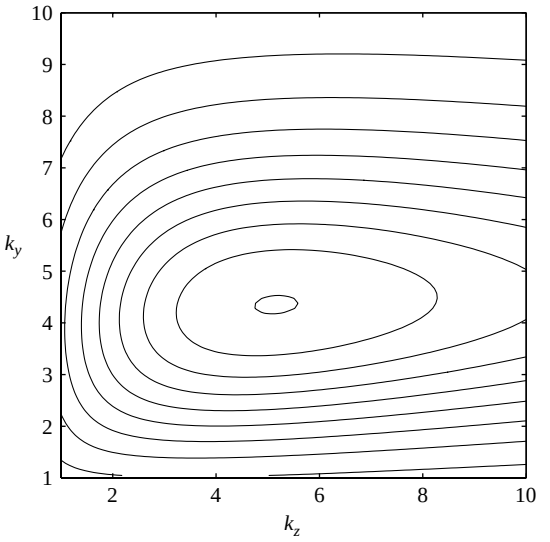

FIGURE 8. The coupling coefficient for $R = 1000$, $k_x = 0.32$. Contour levels correspond to $0.4 \leqslant \Theta \leqslant 2.8$ at an increment of 0.3.

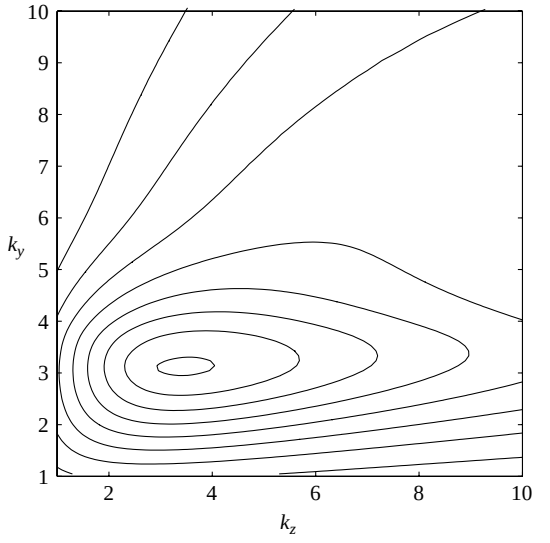

FIGURE 9. Evaluation of the coupling coefficient for $R = 1000$, $k_x = 0.032$. Contour levels correspond to $6 \leqslant \Theta \leqslant 34$ at an increment of 4.

of the disturbance, in the denominator. These two competing physical phenomena set the optimal k_y.

The spanwise wavenumber is explicitly included in the numerator of the coupling coefficient. It also contributes to the decay rate, $\omega_i = -(k_x^2 + k_z^2 + k_y^2)/R$. Assuming the inner product term has little dependence on k_z, the maximum coupling coefficient is then attained at $k_z^2 \simeq k_x^2 + k_y^2$.

A similar plot is shown for $k_x = 0.032$ in figure 9. Qualitatively, this shows similar behaviour to the previous case, $k_x = 0.32$. However, the contour levels are at larger

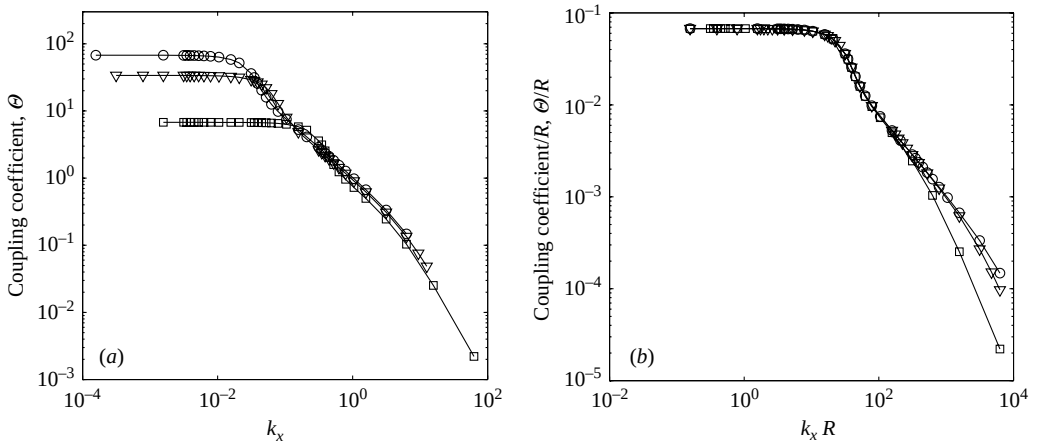

FIGURE 10. The coupling coefficient evaluated at the optimal $k_y^*(k_x), k_z^*(k_x)$. The three curves correspond to: ○, $R = 1000$; ▽, $R = 500$; □, $R = 100$.

amplitude. This is due to enhanced penetration depth associated with lower k_x, corresponding to the observation that lower frequencies penetrate deeper into the boundary layer. Also note that the optimal k_y, k_z values are shifted. The lower k_y is expected since at lower k_x the eigenfunctions penetrate deeper into the boundary layer. Therefore, increasing k_y causes a penalty from the increased decay rate, with little gain from improved penetration. The optimal k_z is also reduced, which implies that the effect of the spanwise wavenumber is consistent with the prediction based on $k_z^2 \simeq k_x^2 + k_y^2$.

The existence of wall-normal k_y^* and spanwise k_z^* optima is now established. Next, we consider the dependence of the coupling coefficient on the streamwise wavenumber. For every k_x, the optimal $k_y^*(k_x)$ and $k_z^*(k_x)$ were obtained, and the coupling coefficient, $\Theta(k_x, k_y^*(k_x), k_z^*(k_x))$, evaluated (see figure 10). The results illustrate the favourable effect of reduced streamwise wavenumber, due in part to enhanced penetration depth, and lower decay rate. When the streamwise wavenumber reaches a lower threshold, k_x^l, further reduction has little influence on the coupling coefficient. In the region $k_x \leqslant k_x^l$, the penetration depth within the boundary layer is maximum. Also, penetration becomes independent of k_y. The optimal k_y^* is then fixed according to $k_y^*(k_x \leqslant k_x^l) = k_y^*(k_x^l)$.

When plotted as Θ/R versus $k_x R$, as in figure 10(*b*), the coupling coefficient is relatively independent of R. The scaling of k_x is suggested by (4.4). The decay rate, in the denominator of the definition of Θ (5.2), varies as $\omega_i \propto 1/R$; this is the origin of the scaling of Θ. The scaled plot shows residual R dependence at short wavelengths. These are the disturbances that do not enter the boundary layer; they collapse in the unscaled form, figure 10(*a*).

Lengths are normalized by boundary layer thickness and $R = U_\infty \delta/\nu$. It follows that k_x and R will become small near the origin of the boundary layer. Since k_x plays the role of a frequency – following Taylor's hypothesis – all modes become low frequency as $\delta \to 0$, and are penetrating; but because $R \to 0$ they also decay rapidly. Hence, disturbances near the leading edge decay (Jacobs & Durbin 2000), and the coupling that leads to boundary layer jets and transition is local, in the downstream region (Leib *et al.* 1999).

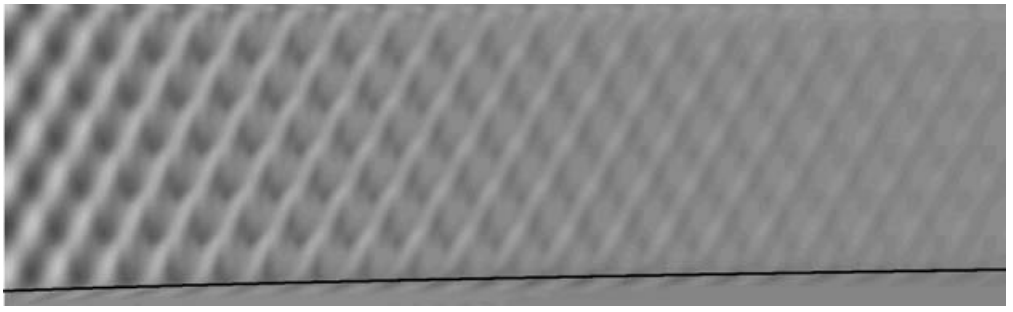

FIGURE 11. Instantaneous contours of streamwise velocity fluctuation ($-0.1 \leqslant u \leqslant 0.1$). The streamwise extent shown is $0.4 \times 10^5 \leqslant R_x \leqslant 2.4 \times 10^5$. The wall-normal coordinate $0 \leqslant y \leqslant 10$ is enlarged by a factor of 3. Line shows δ. Inlet mode: $\omega = 0.64$, $k_y = \pi/3$, $k_z = \pi$, $\Theta = 0.19$.

5.2. *Boundary layer streaks*

The *coupling coefficient*, as defined in (5.2), favours low-frequency modes. These disturbances have low decay rates and are able to penetrate shear regions. Low-frequency perturbations are also associated with the formation of streaks in boundary layer flows. Therefore, the *coupling coefficient* can be used to quantify the ability of an Orr–Sommerfeld disturbance to generate breathing modes within the boundary layer.

For example, consider the two modes with wavenumber vectors $\omega = 0.64$, $k_y = \pi/3$, $k_z = \pi$ and $\omega = 0.032$, $k_y = \pi$, $k_z = 4.7$. The former has a lower coupling coefficient, $\Theta = 0.19$, due to its higher spatial decay rate and lower penetration depth. As a result, it is not expected to generate any boundary layer streaks. The latter mode has a much larger coefficient, $\Theta = 32.5$, and hence is expected to generate perturbation jets inside the boundary layer.

The deductions based on the coupling coefficients are verified using direct numerical simulation of the full Navier–Stokes equations. The Orr–Sommerfeld mode is prescribed at the inlet located at $R = 10^3$, and its development followed downstream. The instantaneous fields due to the evolution of these modes are shown in figures 11 and 12. The numerical results confirm the above predictions based on the coupling coefficient.

Figure 11 is a vertical section, illustrating that the high-frequency low-coupling mode does not penetrate the boundary layer, but simply decays. Since the coupling coefficient characterizes the local interaction of free-stream perturbations with the boundary layer, it is therefore instructive to consider the downstream evolution of Θ. The inlet condition $R = 10^3$, $\omega = 0.64$ can be located on figure 10(*a*) – Taylor's hypothesis is used to replace ω by k_x. The inlet mode is clearly in the sheltered regime ($k_x > k_x^l$), where Θ curves collapse and are independent of any downstream increase in Reynolds number. Meanwhile, based on the local scaling of the boundary layer, the local wavenumber k_x increases downstream, and the coupling coefficient drops. The combined effect of a decreasing Θ, and of the decay in free-stream intensity, is an insignificantly perturbed boundary layer. This is clear in the numerical simulation (figure 11).

Now, consider the results for the low-frequency large-coupling mode. Figure 12 is a planform, showing elongated disturbances in the boundary layer. The streaks initially intensify downstream due to lift-up, followed by viscous decay. This should be contrasted to the behaviour of the free-stream disturbance which simply decays. These results are consistent with the prediction based on the coupling coefficient

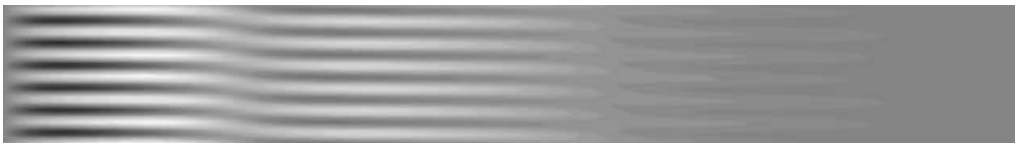

FIGURE 12. Instantaneous contours of streamwise velocity fluctuation ($-0.3 \leqslant u \leqslant 0.3$) evaluated at $y/\delta_0 = 0.58$. The streamwise extent shown is $0.4 \times 10^5 \leqslant R_x \leqslant 2.4 \times 10^5$. The spanwise coordinate $0 \leqslant z \leqslant 8$ is enlarged by a factor of 3. Inlet mode: $\omega = 0.032$, $k_y = \pi$, $k_z = 4.7$, $\Theta = 32.5$.

of the inflow mode. The inflow disturbance, with $k_x R = 32$, can be located near the threshold for fully penetrating disturbances in figure 10(*b*).

It is interesting to consider an inflow disturbance with $k_x R < 10$, and track the spatial development of the coupling coefficient, which is best described using figure 10(*b*). Initially, $k_x R$ is below the threshold for fully penetrating disturbances. Therefore, the penetrating Orr–Sommerfeld mode induces a boundary layer response, and streaks start to develop. Downstream, two regimes can be identified. Initially, based on local scaling, the product $k_x R$ increases, but Θ/R is unaffected, and therefore the coupling coefficient is larger. In the second regime, further downstream, the product $k_x R$ becomes much larger than the threshold value, shear sheltering is effective, and the coupling coefficient starts to drop. As a result of a decreasing Θ and lower intensity, the free-stream disturbance can no longer induce a response inside the boundary layer. This is clear in figure 12 where, downstream of the viscously decaying Klebanoff modes, the boundary layer is unperturbed.

A word of caution is in order when considering the coupling coefficient for low-frequency modes. Evaluating Θ for Orr–Sommerfeld modes ignores non-parallel effects which become important in the long-wavelength limit (Leib *et al.* 1999). However, in the numerical simulations, the Orr–Sommerfeld modes were only applied as an inlet condition. The development of the streaks, which is sensitive to non-parallel effects, was computed with the full Navier–Stokes equations.

6. Bypass transition

Numerical simulations with the full Navier–Stokes equations are used to investigate the coupling further. To this end, modes are specified at the inflow, and their evolution is followed downstream. In this section, the connection of the linear analysis to bypass transition is investigated. In each case, disturbances will be characterized by their coupling coefficient.

The incompressible Navier–Stokes equations are solved using a fractional step algorithm on a staggered grid with a local volume flux formulation (Rosenfeld, Kwak & Vinokur 1991). The convective terms are treated explicitly using Adams–Bashforth time advancement. The pressure and diffusion terms are advanced by implicit Euler and Crank–Nicolson differencing, respectively.

The computational domain, normalized by the inlet δ, is $360 \times 20 \times 16$ in the streamwise, wall-normal, and spanwise directions. The streamwise extent corresponds to $0.4 \times 10^5 < R_x < 4 \times 10^5$, where $R_x = U_\infty x/\nu$. The simulations are performed on a Cartesian grid, uniform in both x- and z-coordinates, and clustered near the wall in the y-direction. The grid resolution is equivalent to the DNS mesh of Jacobs & Durbin (2000).

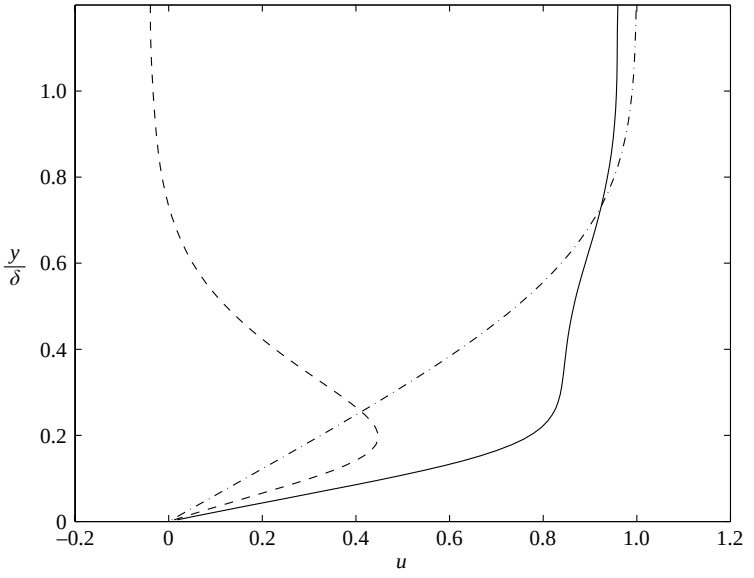

FIGURE 13. Velocity profile in the wall-normal direction at downstream location $R_x = 6.9 \times 10^4$. Inlet fluctuation is a single Orr–Sommerfeld mode with large coupling coefficient: $\omega = 0.032$, $k_y = \pi$, $k_z = 4.7$, $\Theta = 32.5$. ——, Total streamwise velocity; —·—, mean streamwise velocity; - - -, streamwise velocity perturbation.

The inflow is a superposition of the Blasius solution and a fluctuating component due to Orr–Sommerfeld mode(s)

$$\boldsymbol{u}_{inflow} = \boldsymbol{U}_{Blasius} + \epsilon \sum_{modes} \mathrm{Re}\left\{ \frac{1}{k_x^2 + k_z^2} \begin{bmatrix} \mathrm{i}k_x \mathrm{d}\phi/\mathrm{d}y \\ (k_x^2 + k_z^2)\phi \\ \mathrm{i}k_z \mathrm{d}\phi/\mathrm{d}y \end{bmatrix} \mathrm{e}^{\mathrm{i}(\pm k_z z - \omega t)} \right\}.$$

In each simulation, the amplitude of the wall-normal velocity fluctuation, ϵ, is chosen such that $v_{rms} = 3\%$ at the inflow plane. This choice is motivated by the direct dependence of lift-up, and hence of boundary layer streaks, on the wall-normal perturbation. Keeping the inflow v_{rms} constant among simulations allows direct comparison.

The coupling coefficient measures the ability of perturbations to penetrate the boundary layer and produce streaks. This connection was demonstrated in the previous section. DNS of a single inlet Orr–Sommerfeld mode were contrasted for small and large coupling; see figures 11 and 12. Here, the results for large coupling are considered further.

Figures 13 and 14 show the instantaneous u-velocity profile at downstream locations $R_x = 6.9 \times 10^4$ and $R_x = 9.1 \times 10^4$ respectively. In figure 13, the total velocity profile is inflectional. However, it is still inviscidly stable according to Fjortoft's criterion because the inflection point is a vorticity minimum. Since the boundary layer is continuously forced by the free-stream fluctuation, the forward and backward perturbation jets intensify further downstream, and the inflectional velocity profile becomes unstable (figure 14). Strictly, the inflection point theorem and Fjortoft's criterion apply to steady two-dimensional flow. They are invoked here non-rigorously, on the grounds that large-scale low-frequency disturbances are under consideration.

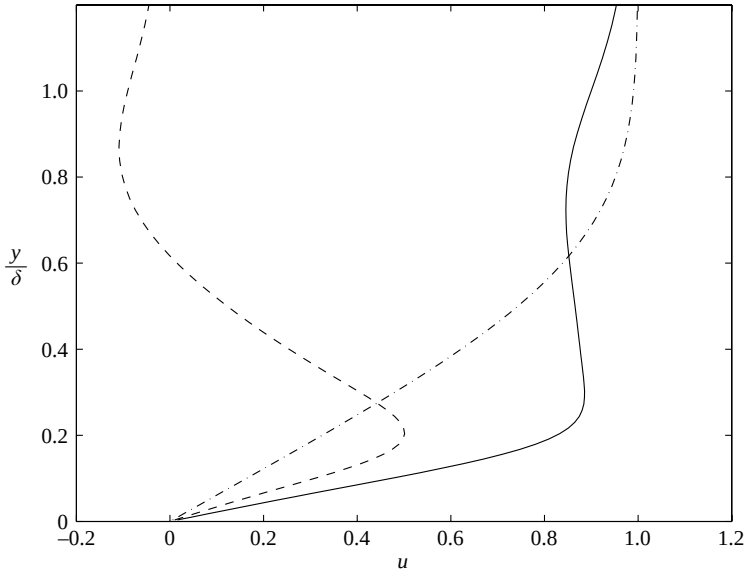

FIGURE 14. As figure 13 but at downstream location $R_x = 9.1 \times 10^4$.

FIGURE 15. Instantaneous contours of streamwise velocity fluctuation ($-0.3 \leqslant u \leqslant 0.3$). The plane is at $y/\delta = 0.8$. The spanwise coordinate is enlarged by a factor of 3. Inlet modes: $\omega = 0.032$, $k_y = \pi$, $k_z = 4.7$, $\Theta = 32.5$ and $\omega = 0.064$, $k_y = 4\pi/3$, $k_z = 3.5$, $\Theta = 10.1$.

The bypass transition scenario proposed in Wu *et al.* (1999) and Jacobs & Durbin (2000) involves a *Kelvin–Helmholtz* type of instability, whereby high-frequency disturbances in the free stream trigger transition of the inflectional profiles near the top of the boundary layer. In order to study this, two Orr–Sommerfeld modes are prescribed at the inlet to the domain. A number of cases were tested, and transition was observed in many of these calculations. Evidence in support of the proposed transition scenario is obtained by examining the earlier stages of spot inception in the transitional cases.

6.1. *Pairwise mode interactions*

Numerical experiments were first performed for inlet pairs of Orr–Sommerfeld modes that have comparable coupling coefficients. When both modes have significant coupling, streaks are formed inside the boundary layer. An instantaneous field due to a pair of such modes is shown in figure 15. The perturbation jets initially intensify downstream due to lift-up. This is followed by viscous decay, and transition is not observed within the computational domain.

When both inlet modes have weak coupling coefficients, strong perturbation jets are absent from the boundary layer. Consider for example the two modes of figure 16. The higher frequency has small penetration depth, and hence does not affect the boundary layer. The other mode has improved, yet still limited, penetration, and a higher decay rate. As a result, it has a small coupling coefficient, and should decay downstream

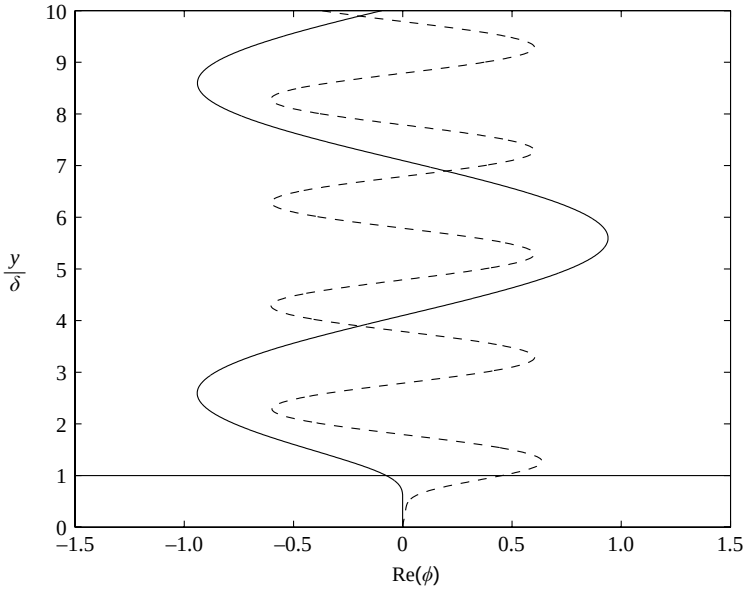

FIGURE 16. Two inlet modes with low coupling coefficients: ——, $\omega = 0.64$, $k_y = \pi/3$, $k_z = \pi$, $\Theta = 0.19$; - - -, $\omega = 0.32$, $k_y = \pi$, $k_z = 1.96$, $\Theta = 1.63$.

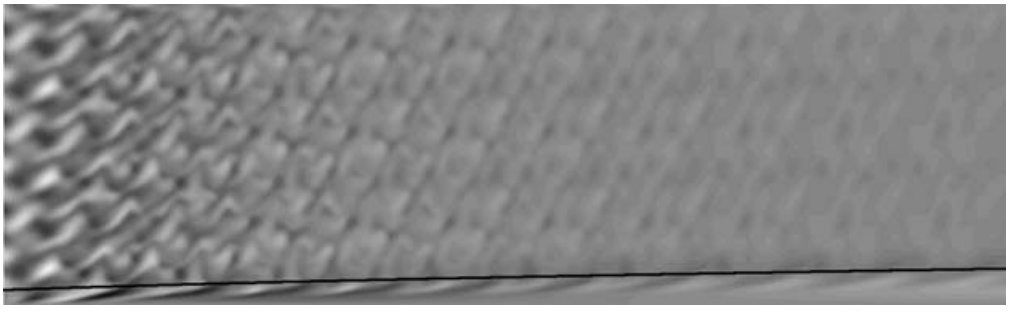

FIGURE 17. Instantaneous contours of streamwise velocity fluctuation ($-0.1 \leqslant u \leqslant 0.1$). The streamwise extent shown is $0.4 \times 10^5 \leqslant R_x \leqslant 2.4 \times 10^5$. The wall-normal coordinate $0 \leqslant y \leqslant 10$ is enlarged by a factor of 3. Line shows δ. Inlet modes: $\omega = 0.64$, $k_y = \pi/3$, $k_z = \pi$, $\Theta = 0.19$ and $\omega = 0.32$, $k_y = \pi$, $k_z = 1.96$, $\Theta = 1.63$.

without the generation of streaks. These predictions are verified using DNS; a plot of the instantaneous streamwise velocity perturbation is shown in figure 17. The disturbance within the boundary layer, due to the slightly penetrating mode, does not exhibit any significant growth – consistent with the small coupling coefficient. Instead, it decays and is qualitatively similar to the free-stream perturbation.

Further simulations were performed to test the case where both inlet Orr–Sommerfeld modes have low or large coupling coefficient. In all cases where both modes had low coupling coefficients, no streaks were observed because shear sheltering prohibited the Orr–Sommerfeld disturbances from penetrating the boundary layer. When the inlet modes both had large coupling, streaks were formed, and the skin friction was slightly above the laminar level. Still, none of these cases transitioned, or developed turbulent spots. It takes only two modes at the inlet to provoke transition;

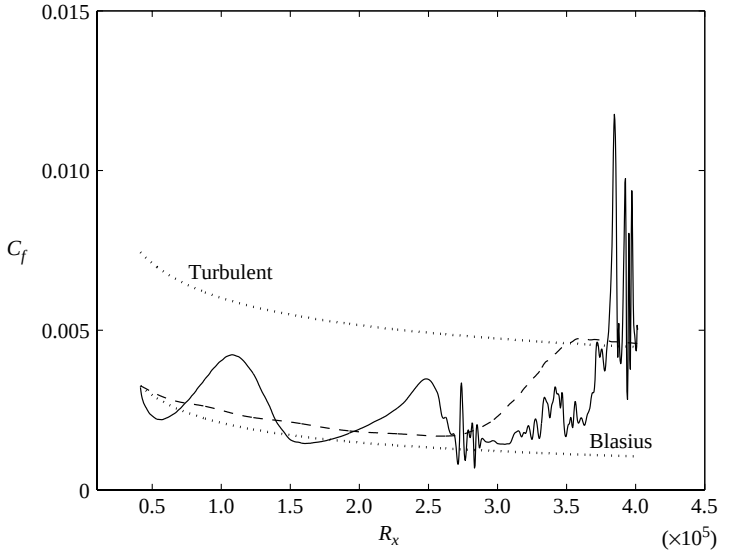

FIGURE 18. Instantaneous (——) and time-averaged (- - -) skin friction profiles. Inlet modes: $\omega = 0.032$, $k_y = 1.87$, $k_z = 2\pi/3.2$, $\Theta = 17.4$ and $\omega = 0.64$, $k_y = \pi/3$, $k_z = \pi$, $\Theta = 0.19$.

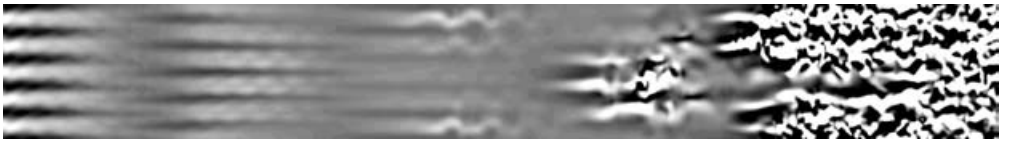

FIGURE 19. Instantaneous v contours corresponding to figure 18. The plane is $y/\delta_0 = 0.5$. The spanwise coordinate is enlarged by a factor of 3.

but they must be one at low frequency, with strong coupling, and one at high frequency.

When one of the modes was strongly coupled, and the other weakly coupled, transition was observed. Figures 18 and 20 show the instantaneous and time-averaged skin friction for two of these transitional cases. In both, the skin friction starts at the Blasius level. Inside the domain, the forward and backward perturbation jets are formed due to the Orr–Sommerfeld mode that has large coupling. Lift-up causes the backward jets to rise inside the boundary layer, while the forward jets stay closer to the wall. This causes an increase in the skin friction coefficient as illustrated in the figures. For the case with larger coupling, the increase in skin friction is more pronounced due to stronger jets. Also, this case transitions earlier because an inflectional profile is achieved early upstream.

The instantaneous skin friction profiles show a patch of turbulence upstream of the fully turbulent region. The instantaneous velocity field corresponding to this skin friction profile is shown in figures 19 and 21, where the streaks, turbulent spots, and transition are evident.

In experiments on bypass transition (Westin *et al.* 1994), and also DNS (Jacobs & Durbin 2000), the increase in skin friction due to forward perturbation jets is not as intense as observed in figure 20. This suggests that an optimal disturbance, or one

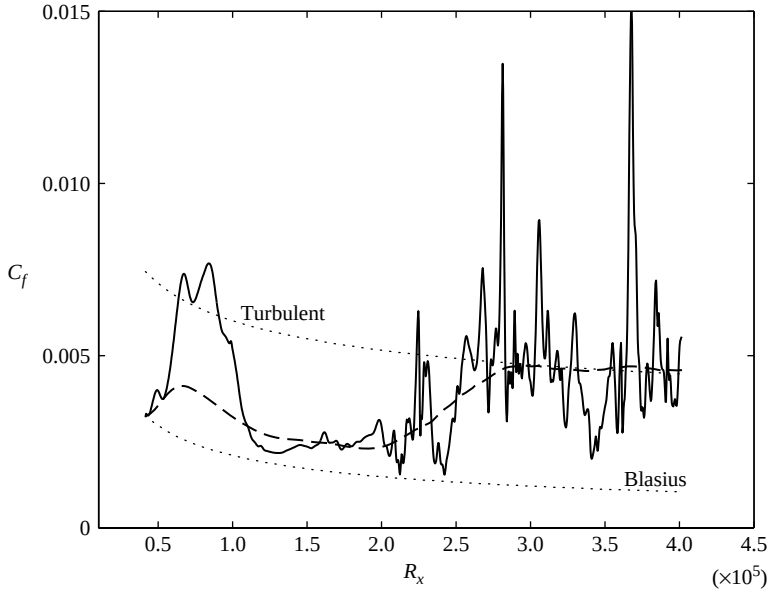

FIGURE 20. Instantaneous (——) and time-averaged (- - -) skin friction profiles. Inlet modes: $\omega = 0.032, k_y = \pi, k_z = 4.7, \Theta = 32.5$ and $\omega = 0.32, k_y = \pi, k_z = 2.7, \Theta = 2.0$.

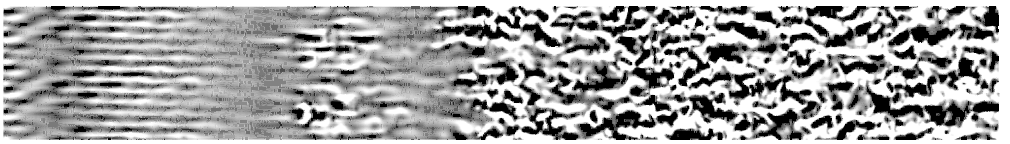

FIGURE 21. Instantaneous v contours corresponding to figure 20. The plane is $y/\delta_0 = 0.5$. The spanwise coordinate is enlarged by a factor of 3.

with highest coupling coefficient, is not needed. It is sufficient to have a disturbance that generates lifting backward jets, and as a result, an inflectional velocity profile towards the edge of the boundary layer. This profile is then acted on by the higher frequency non-penetrating perturbation.

6.2. *Spot inception and Kelvin–Helmholtz type of instability*

In order to better understand the process of turbulent spot inception, we examine the earlier stages that lead to the formation of the turbulent patches. Figure 22 is a time sequence showing the high-frequency instability of the elevated backward perturbation jets. The time sequence is extracted from the simulation presented in figures 18 and 19. The background contours show the vertical velocity disturbance; light contours correspond to positive v and dark regions to negative values.

Frame (*a*) shows the forward jet close to the wall; it is due to downward displacement of high-speed fluid (dark v-contours). The backward perturbation jet, due to upward displacement of low-speed fluid from near the wall, is elevated towards the edge of the boundary layer. The frequency of those 'breathing modes' corresponds to the low-frequency inflow disturbance, $\omega = 0.032$. Higher harmonics of the inflow disturbance and also interaction modes can be generated by the non-linearity. However, the dominant frequency for the boundary layer disturbance agrees with the inflow large-coupling mode. This should be contrasted to Jacobs & Durbin

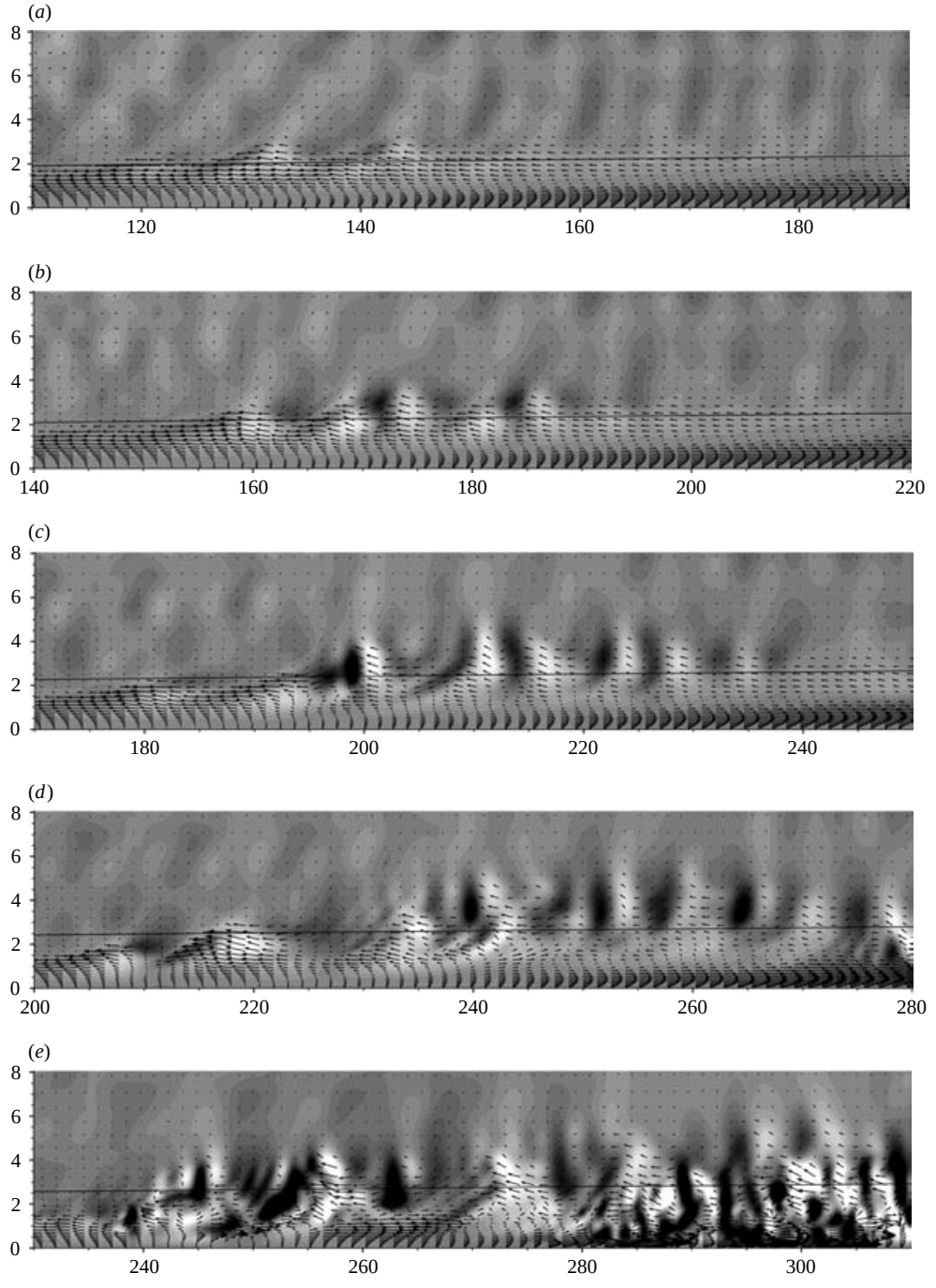

FIGURE 22. Perturbation velocity vectors in the (x, y)-plane. Time sequence showing the Kelvin–Helmholtz type instability of elevated backward perturbation jets and the inception of a turbulent spot. The sequence is extracted from the simulation presented in figures 18 and 19. The vertical scale has been expanded by a factor of 2; vectors are separated by 4 grid points. The background contours show the v-component ($-0.05 \leqslant v \leqslant 0.05$). The viewing window is translated at $\frac{2}{3}U_\infty$ in order to follow the development of the turbulent spot.

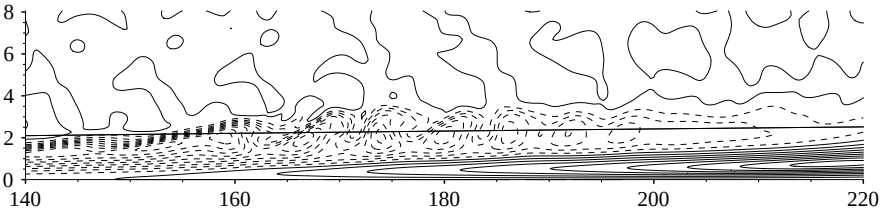

FIGURE 23. Instantaneous contours of streamwise velocity fluctuation ($-0.3 \leqslant u \leqslant 0.3$) corresponding to figure 22(*b*). Dashed contours indicate negative values. Line shows δ.

(2000) where the streaks have a much lower frequency than any of the inflow disturbances – in that case, they are generated by the interactions of a whole spectrum of modes.

Small regions of undulation in the vertical velocity contours can be observed near the edge of the boundary layer, on top of the backward jet. These perturbations are pronounced in figure 22(*b*). The corresponding u-contours are shown in figure 23, and provide a better representation of the instability. The streamwise wavelength of these undulations is approximately 6.7 times inflow δ, and they convect downstream at $\frac{2}{3}U_\infty$. Therefore, their temporal frequency is in agreement with the high-frequency inflow mode $\omega = 0.64$. Their short wavelength implies a low coupling coefficient and poor penetration depth due to shear sheltering. Figure 23 confirms these predictions; the high-frequency disturbance only affects the elevated backward perturbation jet. The near-wall, forward jet is unaltered by the high-frequency free-stream disturbance. Figure 23 also displays a marked similarity between the secondary instability of the backward perturbation jets and the early stages of Kelvin–Helmholtz instability.

Figures 22(*c*)–22(*e*) capture the evolution of the secondary instability into a turbulent spot. The flow region displayed moves downstream at $\frac{2}{3}U_\infty$ in order to follow the growing instability. The streamwise and wall-normal extents of the high-frequency disturbance clearly grow in time. The spanwise extent, not shown in this figure, also increases. As the instability travels downstream, it intensifies and finally erupts into a turbulent spot. The convected turbulent patch spreads, and merges with the downstream fully turbulent flow as illustrated in figure 19.

7. Conclusion

The local interaction between free-stream disturbances and the boundary layer shear is important in the study of bypass transition. Experiments and numerical simulations both suggest low-frequency disturbances are more effective at penetrating the boundary layer, and generating 'breathing' or Klebanoff modes. High-frequency disturbances are limited to the free stream leaving the boundary layer unperturbed. This behaviour is captured by the shape of the continuous Orr–Sommerfeld and Squire modes. These eigensolutions are oscillatory in the free stream, and decay inside the boundary layer. Eigenmodes of the piecewise-linear profile demonstrate an analytic dependence of penetration depth on the wavenumber vector, local Reynolds number R, and local shear.

The effect of the wall-normal wavenumber k_y on penetration depth is particularly interesting. The solution to an initial value problem shows that an Orr–Sommerfeld disturbance forces Squire's equation resonantly. The response is a packet of Squire modes with varying k_y, and, hence, varying penetration into the boundary layer. Incomplete cancellation of this superposition of the Squire eigenfunctions

gives rise to Klebanoff modes. A coupling coefficient was defined to characterize the local interaction of continuous Orr–Sommerfeld modes and the boundary layer. The coefficient captures the variation in penetration depth, and also the propensity of Orr–Sommerfeld forcing to generate boundary layer streaks.

In order to investigate the coupling further, numerical simulations of the full Navier–Stokes equations were performed for a pair of inflow modes. The complete transition process is realizable through the interaction of one strongly coupled and one weakly coupled mode. The low-frequency large-coupling inflow disturbance generates breathing modes inside the boundary layer. The backward perturbation jets lift away from the wall, towards the edge of the boundary layer. The inflectional velocity profile then becomes susceptible to short-wavelength instabilities of the Kelvin–Helmholtz type, triggered by the high-frequency free-stream disturbance. These instabilities intensify downstream, and burst into turbulent spots.

This work is sponsored by the National Science Foundation and by the Department of Energy, under their ASC program.

Appendix. Solution of the initial value problem

The initial value problem for the case of Squire modes, generated by single Orr–Sommerfeld mode forcing, gives a theoretical basis for the coupling coefficient that was used in the text to describe the effectiveness of disturbances in penetrating, and perturbing, the shear layer. Linear theory is well developed (Grosch & Salwen 1978; Gustavsson 1979; Schmid & Henningson 2001). We describe the solution to a linear initial value problem to provide a connection between linear theory and nonlinear mode interactions, and to provide a new perspective on Klebanoff modes.

Consider the general problem of a small disturbance to a parallel mean flow. The disturbance can be expanded in Fourier components:

$$v_{\boldsymbol{\kappa}}(y,t) = \int_{k_x}\int_{k_z} v(\boldsymbol{x},t)\mathrm{e}^{-\mathrm{i}k_x x}\mathrm{e}^{-\mathrm{i}k_z z}\,\mathrm{d}x\,\mathrm{d}z,$$

$$\eta_{\boldsymbol{\kappa}}(y,t) = \int_{k_x}\int_{k_z} \eta(\boldsymbol{x},t)\mathrm{e}^{-\mathrm{i}k_x x}\mathrm{e}^{-\mathrm{i}k_z z}\,\mathrm{d}x\,\mathrm{d}z.$$

Since the eigenfunctions for the Orr–Sommerfeld and Squire equations, as defined by (2.3), are complete for a given horizontal wavenumber vector $\boldsymbol{\kappa}=(k_x,k_z)$, the disturbance velocity and normal vorticity can be expanded in these eigenfunctions:

$$\left.\begin{aligned} v_{\boldsymbol{\kappa}}(y,t) &= \sum_{n=1}^{N_{OS,\boldsymbol{\kappa}}} a_{\boldsymbol{\kappa},n}(t)\phi_{\boldsymbol{\kappa},n}(y) + \int_{k_y} a_{\boldsymbol{\kappa},k_y}(t)\phi_{\boldsymbol{\kappa},k_y}(y)\,\mathrm{d}k_y,\\ \eta_{\boldsymbol{\kappa}}(y,t) &= \sum_{n=1}^{N_{SQ,\boldsymbol{\kappa}}} b_{\boldsymbol{\kappa},n}(t)\chi_{\boldsymbol{\kappa},n}(y) + \int_{k_y} b_{\boldsymbol{\kappa},k_y}(t)\chi_{\boldsymbol{\kappa},k_y}(y)\,\mathrm{d}k_y. \end{aligned}\right\} \tag{A 1}$$

Subscript n denotes the discrete eigensolutions, while k_y refers to the continuous spectrum.

In order to extract the Squire response to a specific Orr–Sommerfeld mode $(\boldsymbol{\kappa},\tilde{k}_y)$, we choose

$$a_{\boldsymbol{\kappa},k_y}(t) = a_{\boldsymbol{\kappa},\tilde{k}_y}\delta(k_y-\tilde{k}_y)$$

so that

$$v_{\boldsymbol{\kappa}}(y,t) = \int_{k_y} a_{\boldsymbol{\kappa},\tilde{k}_y}(t)\delta(k_y-\tilde{k}_y)\phi_{\boldsymbol{\kappa},k_y}(y)\,\mathrm{d}k_y = a_{\boldsymbol{\kappa},\tilde{k}_y}(t)\phi_{\boldsymbol{\kappa},\tilde{k}_y}(y). \tag{A 2}$$

Therefore the only vertical velocity disturbance present in the flow is

$$v(\boldsymbol{x}, t) = a_{\boldsymbol{\kappa},\tilde{k}_y}(t)\phi_{\boldsymbol{\kappa},\tilde{k}_y}(y)\mathrm{e}^{\mathrm{i}k_x x}\mathrm{e}^{\mathrm{i}k_z z}.$$

The tilde over variables indicates that they are properties of the prescribed Orr–Sommerfeld mode. Direct substitution of (A 2) in the Orr–Sommerfeld equation results in

$$d_t a_{\boldsymbol{\kappa},\tilde{k}_y}(t) = -\mathrm{i}\omega_{os,\tilde{k}_y} a_{\boldsymbol{\kappa},\tilde{k}_y}(t)$$

and hence

$$a_{\boldsymbol{\kappa},\tilde{k}_y}(t) = a_{\boldsymbol{\kappa},\tilde{k}_y,0}\mathrm{e}^{-\mathrm{i}\omega_{os,\tilde{k}_y}t}.$$

Now, it remains to solve the forced Squire equation. Properties of the adjoint problem are used to separate the Squire response into its different eigenfunctions. The adjoint eigenvalue problem is defined as

$$\begin{aligned} L^{\dagger}_{OS}\phi^{\dagger}_m &= \mathscr{L}^{\dagger}\phi^{\dagger}_m - \mathrm{i}\omega^{\dagger}_m\phi^{\dagger} = 0, \\ L^{\dagger}_{SQ}\chi^{\dagger}_n &= \mathscr{S}^{\dagger}\chi^{\dagger}_n - \mathrm{i}\omega^{\dagger}_n\chi^{\dagger} = 0. \end{aligned}$$

Since the eigenvalues of the original problem (2.3) are distinct ($\omega_m \neq \omega_n$ for $m \neq n$), the adjoint eigenfunctions satisfy

$$\begin{aligned} \omega^{\dagger}_m &= \omega^{\star}_m, & \omega^{\dagger}_{k_y} &= \omega^{\star}_{k_y}, \\ \langle\phi^{\dagger}_m, \phi_n\rangle &= \delta_{mn}, & \langle\phi^{\dagger}_{k_y}, \phi_{k'_y}\rangle &= \delta(k_y - k'_y), \\ \langle\chi^{\dagger}_m, \chi_n\rangle &= \delta_{mn}, & \langle\chi^{\dagger}_{k_y}, \chi_{k'_y}\rangle &= \delta(k_y - k'_y). \end{aligned}$$

Using the orthogonality properties of the adjoint, the coefficients of the normal vorticity are obtained from

$$\begin{aligned} b_{\boldsymbol{\kappa},m}(t) &= \langle\chi^{\dagger}_m, \eta_{\boldsymbol{\kappa}}(y, t)\rangle, \\ b_{\boldsymbol{\kappa},k_y}(t) &= \langle\chi^{\dagger}_{k_y}, \eta_{\boldsymbol{\kappa}}(y, t)\rangle. \end{aligned}$$

Since $\eta_{\boldsymbol{\kappa}}$ satisfies the Squire equation, the above leads to

$$\begin{aligned} d_t b_{\boldsymbol{\kappa},m}(t) &= -\langle\chi^{\dagger}_m, \mathscr{S}\eta_{\boldsymbol{\kappa}}(y, t)\rangle - \langle\chi^{\dagger}_m, \mathscr{C}\phi_{\boldsymbol{\kappa},\tilde{k}_y}(y)a_{\boldsymbol{\kappa},\tilde{k}_y,0}\mathrm{e}^{-\mathrm{i}\omega_{os,\tilde{k}_y}t}\rangle, \\ d_t b_{\boldsymbol{\kappa},k_y}(t) &= -\langle\chi^{\dagger}_{k_y}, \mathscr{S}\eta_{\boldsymbol{\kappa}}(y, t)\rangle - \langle\chi^{\dagger}_{k_y}, \mathscr{C}\phi_{\boldsymbol{\kappa},\tilde{k}_y}(y)a_{\boldsymbol{\kappa},\tilde{k}_y,0}\mathrm{e}^{-i\omega_{os,\tilde{k}_y}t}\rangle. \end{aligned}$$

Expanding $\eta_{\boldsymbol{\kappa}}(y, t)$ according to (A 1) and using the orthogonality properties of the adjoint leads to

$$\left.\begin{aligned} d_t b_{\boldsymbol{\kappa},m}(t) &= -\mathrm{i}\omega_{\boldsymbol{\kappa},m}b_{\boldsymbol{\kappa},m}(t) - \langle\chi^{\dagger}_m, \mathscr{C}\phi_{\boldsymbol{\kappa},\tilde{k}_y}(y)\rangle a_{\boldsymbol{\kappa},\tilde{k}_y,0}\mathrm{e}^{-\mathrm{i}\omega_{os,\tilde{k}_y}t}, \\ d_t b_{\boldsymbol{\kappa},k_y}(t) &= -\mathrm{i}\omega_{\boldsymbol{\kappa},k_y}b_{\boldsymbol{\kappa},k_y}(t) - \langle\chi^{\dagger}_{k_y}, \mathscr{C}\phi_{\boldsymbol{\kappa},\tilde{k}_y}(y)\rangle a_{\boldsymbol{\kappa},\tilde{k}_y,0}\mathrm{e}^{-\mathrm{i}\omega_{os,\tilde{k}_y}t}. \end{aligned}\right\} \tag{A 3}$$

Before the solution for $b_{\boldsymbol{\kappa},m}(t)$ and $b_{\boldsymbol{\kappa},k_y}(t)$ is explicitly stated, recall that both the Orr–Sommerfeld and homogeneous Squire eigenvalue problems have the same continuous eigenvalues ω_{k_y}, for a given wavenumber vector $(k_x, k_z, k_y) = (\boldsymbol{\kappa}, k_y)$. Therefore, resonance will take place between the single Orr–Sommerfeld mode and the Squire mode with the same eigenvalue. Taking this resonance into account, the spectral coefficients of the normal vorticity expansion are the solutions to (A 3): for discrete Squire modes

$$b_{\boldsymbol{\kappa},m}(t) = b_{\boldsymbol{\kappa},m}(0)\mathrm{e}^{-\mathrm{i}\omega_{\boldsymbol{\kappa},m}t} - a_{\boldsymbol{\kappa},\tilde{k}_y,0}\langle\chi^{\dagger}_m, \mathscr{C}\phi_{\boldsymbol{\kappa},\tilde{k}_y}(y)\rangle\left[\frac{\mathrm{e}^{-\mathrm{i}\omega_{os,\tilde{k}_y}t} - \mathrm{e}^{-\mathrm{i}\omega_m t}}{-\mathrm{i}(\omega_{os,\tilde{k}_y} - \omega_m)}\right]; \tag{A 4}$$

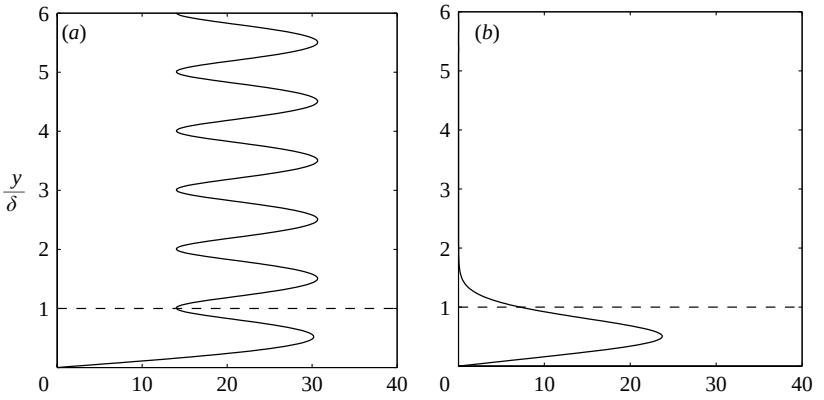

FIGURE 24. Squire mode response to Orr–Sommerfeld forcing at $R = 1000$, $k_x = 0.01$, $\tilde{k}_y = \pi$, $k_z = \pi$. The response is evaluated at $t = 60$. (*a*) Abscissa is the secular term $b_{\boldsymbol{\kappa},\tilde{k}_y}\chi_{\boldsymbol{\kappa},\tilde{k}_y}(y)$; (*b*) Abscissa is a discrete evaluation of $\int_{\pi/20}^{5\pi} b_{\boldsymbol{\kappa},k_y}\chi_{\boldsymbol{\kappa},k_y}(y)dk_y$.

for continuous Squire modes ($k_y \neq \tilde{k}_y$)

$$b_{\boldsymbol{\kappa},k_y}(t) = b_{\boldsymbol{\kappa},k_y}(0)\mathrm{e}^{-\mathrm{i}\omega_{\boldsymbol{\kappa},k_y}t} - a_{\boldsymbol{\kappa},\tilde{k}_y,0}\left\langle \chi^{\dagger}_{k_y}, \mathscr{C}\phi_{\boldsymbol{\kappa},\tilde{k}_y}(y)\right\rangle \left[\frac{\mathrm{e}^{-\mathrm{i}\omega_{os,\tilde{k}_y}t} - \mathrm{e}^{-\mathrm{i}\omega_{k_y}t}}{-\mathrm{i}(\omega_{os,\tilde{k}_y} - \omega_{k_y})}\right]; \tag{A 5}$$

and for the resonant mode ($k_y = \tilde{k}_y$)

$$b_{\boldsymbol{\kappa},\tilde{k}_y}(t) = b_{\boldsymbol{\kappa},\tilde{k}_y}(0)\mathrm{e}^{-\mathrm{i}\omega_{\boldsymbol{\kappa},\tilde{k}_y}t} - a_{\boldsymbol{\kappa},\tilde{k}_y,0}\left\langle \chi^{\dagger}_{\tilde{k}_y}, \mathscr{C}\phi_{\boldsymbol{\kappa},\tilde{k}_y}(y)\right\rangle t\left[\mathrm{e}^{-\mathrm{i}\omega_{os,\tilde{k}_y}t}\right]. \tag{A 6}$$

If one considers the case with no initial vertical vorticity, $\eta_\kappa(y, t = 0) = 0$, then $b_{\boldsymbol{\kappa},m}(0) = b_{\boldsymbol{\kappa},k_y}(0) = 0$.

Properties of the solution to the initial value problem

The solution to the temporal problem of normal vorticity generation due to Orr–Sommerfeld forcing is given by substituting (A 4) to (A 6) into (A 1). The eigenvalue problem used in deriving the solution is given by (2.3). This treatment emphasizes the role of resonance between the Orr–Sommerfeld forcing and the Squire equation, resulting in the secular growth (A 6).

The coupling term $\mathscr{C}$ does not appear as a non-normal contribution to the eigenvalue problem; instead, it is included as forcing in the Squire equation. In the solution (A 5), its contribution is the inner product $\langle \chi^{\dagger}_{k_y}, \mathscr{C}\phi_{\boldsymbol{\kappa},\tilde{k}_y}(y)\rangle$.

In optimal growth analysis, the coupling term $\mathscr{C}$ is treated as part of the matrix operator, as in (2.2). The eigenfunction is the vector variable (ϕ, χ). Then it is not obvious how certain Orr–Sommerfeld forcing induces better coupling to Squire modes than others. By contrast, in the solution given by (A 5), the amplitude of coupling is proportional to the penetration depth of the Orr–Sommerfeld mode: the deeper penetrating modes sample more of the mean shear, and hence have larger coupling.

In the case of zero initial vorticity, the Orr–Sommerfeld forcing should generate normal vorticity inside the shear region by tilting mean vorticity. No normal vorticity should contaminate the free stream, except due to diffusion across the edge of the boundary layer. Therefore, the superposition of Squire modes in (A 1) should vanish in the free stream, but not inside the boundary layer.

Figure 24 shows the Squire response to Orr–Sommerfeld forcing at $R = 1000$, $k_x = 0.01$, $\tilde{k}_y = \pi$, $k_z = \pi$. The maximum amplitude of the initial normal velocity disturbance is unity in the free stream,

$$\max\ |v_{\boldsymbol{\kappa}}(t=0)|_{y\to\infty} = \max\ |a_{\boldsymbol{\kappa},\tilde{k}_y}(t=0)\phi_{\boldsymbol{\kappa},\tilde{k}_y}(y)|_{y\to\infty} = 1.$$

The figure shows the response at $t = 60$. Plot (a) is the secular term $b_{\boldsymbol{\kappa},\tilde{k}_y}\chi_{\boldsymbol{\kappa},\tilde{k}_y}(y)$ which oscillates in the free stream. Plot (b) is a numerical evaluation of $\int_{\pi/20}^{5\pi} b_{\boldsymbol{\kappa},k_y}\chi_{\boldsymbol{\kappa},k_y}(y)\,\mathrm{d}k_y$ of equation (A 1). The superposition of eigenmodes is destructive in the free stream. But because penetration into the shear region is wavelength dependent, the disturbance reaches large amplitude inside the boundary layer. Resonant forcing of penetrating modes produces a large response in the boundary layer, but this must be qualified by the observation that all modes are present to cancel the disturbance at large y. Thus, one obtains a perspective that breathing 'modes' can be understood as a superposition of Squire modes.

REFERENCES

Butler, K. M. & Farrell, B. F. 1992 Three-dimensional optimal disturbances in viscous shear flow. *Phys. Fluids* A **4**, 1637–1650.

Drazin, P. & Reid, W. H. 1995 *Hydrodynamic Stability*. Cambridge University Press.

Goldstein, M. E. & Wundrow, D. W. 1998 On the environmental realizability of algebraically growing disturbances and their relation to Klebanoff modes. *Theoret. Comput. Fluid Dyn.* **10**, 171–186.

Grosch, C. E. & Salwen, H. 1978 The continuous spectrum of the Orr–Sommerfeld equation. Part 1. The spectrum and the eigenfunctions. *J. Fluid Mech.* **68**, 33–54.

Gustavsson, L. H. 1979 Initial value problem for boundary layer flows *Phys. Fluids* **22**, 1602–1605.

Hultgren, L. S. & Gustavsson, L. H. 1981 Algebraic growth of disturbances in a laminar boundary layer. *Phys. Fluids* **24**, 1000–1004.

Hunt, J. C. R. & Durbin, P. A. 1999 Perturbed shear layers. *Fluid Dyn. Res.* **24**, 375–404.

Jacobs, R. G. & Durbin, P. A. 1998 Shear sheltering and the continuous spectrum of the Orr–Sommerfeld equation. *Phys. Fluids* **10**, 2006–2011.

Jacobs, R. G. & Durbin, P. A. 2000 Simulations of bypass transition. *J. Fluid Mech.* **428**, 185–212.

Kemp, N. 1951 The laminar three-dimensional boundary layer and a study of the flow past a side edge. MAcS Thesis, Cornell University.

Kendall, J. M. 1991 Studies on laminar boundary layer receptivity to free stream turbulence near a leading edge. In *Boundary Layer Stability and Transition to Turbulence* (ed. X. Reda *et al.*). ASME-FED vol. 114, pp. 23–30.

Klebanoff, P. S. 1971 Effect of free-stream turbulence on a laminar boundary layer. *Bull. Am. Phys. Soc.* **10**, 1323.

Kleiser, L. & Zang, T. A. 1991 Numerical simulation of transition in wall-bounded shear flows. *Annu. Rev. Fluid Mech.* **23**, 495–537.

Leib, S. J., Wundrow, D. & Goldstein, M. E. 1999 Effect of free-stream turbulence and other vortical disturbances on a laminar boundary layer. *J. Fluid Mech.* **380**, 169–203.

Phillips, O. M. 1969 Shear-flow turbulence. *Annu. Rev. Fluid Mech.* **1**, 245–264.

Rosenfeld, M., Kwak, D. & Vinokur, M. 1991 A fractional step solution method for the unsteady incompressible Navier–Stokes equations in generalized coordinate systems. *J. Comput. Phys.* **94**, 102–137.

Schmid, P. J. & Henningson, D. S. 2001 *Stability and Transition in Shear Flows*. Springer.

Westin, K. J. A., Boiko, A. V., Klingmann, B. G. B., Kozlov, V. V. & Alfredsson, P. H. 1994 Experiments in a boundary layer subjected to freestream turbulence. Part 1. Boundary layer structure and receptivity. *J. Fluid Mech.* **281**, 193–218.

Wu, X., Jacobs, R. G., Hunt, J. C. R. & Durbin, P. A. 1999 Simulation of boundary layer transition induced by periodically passing wakes. *J. Fluid Mech.* **398**, 109–153.